

Mathematical Models for Cell Migration with Real-Time Cell Cycle Dynamics

Sean T. Vittadello,¹ Scott W. McCue,¹ Gency Gunasingh,² Nikolas K. Haass,^{2,3} and Matthew J. Simpson^{1,*}

¹School of Mathematical Sciences, Queensland University of Technology, Brisbane, Queensland, Australia; ²The University of Queensland, The University of Queensland Diamantina Institute, Translational Research Institute, Woolloongabba, Brisbane, Queensland, Australia; and

³Discipline of Dermatology, Faculty of Medicine, Central Clinical School, University of Sydney, Sydney, New South Wales, Australia

ABSTRACT The fluorescent ubiquitination-based cell cycle indicator, also known as FUCCI, allows the visualization of the G1 and S/G2/M cell cycle phases of individual cells. FUCCI consists of two fluorescent probes, so that cells in the G1 phase fluoresce red and cells in the S/G2/M phase fluoresce green. FUCCI reveals real-time information about cell cycle dynamics of individual cells, and can be used to explore how the cell cycle relates to the location of individual cells, local cell density, and different cellular microenvironments. In particular, FUCCI is used in experimental studies examining cell migration, such as malignant invasion and wound healing. Here we present, to our knowledge, new mathematical models that can describe cell migration and cell cycle dynamics as indicated by FUCCI. The fundamental model describes the two cell cycle phases, G1 and S/G2/M, which FUCCI directly labels. The extended model includes a third phase, early S, which FUCCI indirectly labels. We present experimental data from scratch assays using FUCCI-transduced melanoma cells, and show that the predictions of spatial and temporal patterns of cell density in the experiments can be described by the fundamental model. We obtain numerical solutions of both the fundamental and extended models, which can take the form of traveling waves. These solutions are mathematically interesting because they are a combination of moving wavefronts and moving pulses. We derive and confirm a simple analytical expression for the minimum wave speed, as well as exploring how the wave speed depends on the spatial decay rate of the initial condition.

INTRODUCTION

The cell cycle consists of a sequence of four distinct phases, namely: gap 1 (G1), synthesis (S), gap 2 (G2), and the mitotic (M) phase (1). The phases G1, S, and G2 are collectively referred to as “interphase”, and involve cell growth and preparation for division. After interphase, the cell enters the mitotic phase and divides into two daughter cells. Although morphological changes associated with cell division can be observed visually during the transition from M to G1, such distinct morphological changes are not possible during transitions between other cell cycle phases (2). Therefore, different techniques are required to study these other cell cycle transitions.

Since 2008, fluorescent ubiquitination-based cell cycle indicator (FUCCI) technology (2) has enabled the visualization of the cell cycle progression from G1 to S/G2/M in individual cells. The FUCCI system consists of two fluorescent

probes in the cell nucleus, or cytoplasm, which emit red fluorescence when the cell is in the G1 phase, or green fluorescence when the cell is in the S/G2/M phase. Before the development of FUCCI it was difficult, if not impossible, to examine the cell cycle dynamics of individual cells beyond the M to G1 transition (2). In contrast, FUCCI allows direct visualization, in real time, of transitions in the cell cycle. This technology is particularly useful for research in cancer biology (3–6), cell biology (7,8), and stem cell biology (9,10).

3D spheroids and 2D scratch assays are commonly used experimental models to study the invasive and proliferative behavior of cancer cells. In combination with FUCCI, these experimental models can be used to examine the cell cycle dynamics of individual cells as a function of position within the spheroid or scratch assay (3,5,6). A major advantage of this method is that two fundamental phenomena associated with malignant invasion, namely cell proliferation and cell migration, can be characterized simultaneously. Previous methods to examine the roles of cell migration and cell proliferation involve pretreating cells with antimetabolic drugs, such as mitomycin-C (11). A major limitation of

Submitted August 11, 2017, and accepted for publication December 21, 2017.

*Correspondence: matthew.simpson@qut.edu.au

Nikolas K. Haass and Matthew J. Simpson contributed equally to this work.

Editor: James Sneyd.

<https://doi.org/10.1016/j.bpj.2017.12.041>

© 2018 Biophysical Society.



these previous methods is that the application of the antimetabolic drug is thought to suppress proliferation without interrupting migration. However, this assumption is questionable, and rarely examined (12). The development of Fucci technology obviates the need for such crude methods to isolate the roles of cell migration and cell proliferation. Instead, Fucci allows us to directly examine the spatial and temporal patterns of cell proliferation within a migrating population. To the best of our knowledge, there are no mathematical models in the literature that have been developed to describe cell migration with Fucci technology. The focus of this work is on cell migration, by which we mean a moving front of a population of cells. These moving fronts are composed of a large number of individual cells that do not maintain cell-to-cell contacts. The formation of the moving front of cells is driven by a combination of cell motility and cell proliferation.

Cell migration involves diffusion, arising from random cell motility, and proliferation of cells (12). Mathematical models describing these processes in a population of cells tend to involve reaction-diffusion equations (13), which are often based on the Fisher-Kolmogorov-Petrovskii-Piskunov (FKPP) equation (14,15),

$$\frac{\partial s}{\partial t} = D \frac{\partial^2 s}{\partial x^2} + \lambda s(1 - s), \quad (1)$$

where $s(x,t) > 0$ is the cell density, $D > 0$ is the diffusion coefficient, and $\lambda > 0$ is the proliferation rate. Here, the dimensional cell density is scaled by the dimensional carrying capacity density, so that the maximum nondimensional cell density is $s(x,t) = 1$. Carrying capacity limited proliferation of cells is described in Eq. 1 with a logistic source term. Equation 1 has been successfully adapted to model many biological processes, such as in vitro cell migration (16–18). A limitation of Eq. 1 is that it considers a single population of cells. For a more realistic situation, where the total population is composed of a number of distinct, interacting subpopulations, it is relevant to consider a model that involves a system of coupled equations that are often related to Eq. 1 (19).

The existence of traveling wave solutions for the FKPP equation is well known (15,20). Constant shape, monotonically decreasing, wavefront traveling wave solutions propagate with a minimum speed, $c_{\min} = 2\sqrt{\lambda D}$ (15,20). Traveling wave solutions are of interest, because experimental observations tend to exhibit moving fronts that can be thought of as a traveling wave (16). The speed of a moving cell front is often the simplest quantitative measurement that can be obtained from an experiment (16,21). Therefore, understanding the relationship between the parameters in the mathematical model and the speed of the traveling wave solution is a useful way to help parameterize the mathematical model to match experimental observations. Traveling wave solutions have also been observed in other mathematical

models of cell migration (16,19,21,22), as well as other reaction-diffusion models related to biological processes (23–26). Most traveling wave solutions take the form of moving wavefronts, which have a monotone profile. Another type of traveling wave solution is a pulse, which is characterized by a nonmonotone profile (23,27).

Here we present, to our knowledge, a new mathematical model of cell migration, which incorporates cell cycle dynamics based on the information provided by Fucci technology in relation to the cell cycle phase. We consider the cells in a particular phase of the cell cycle to make up a distinct subpopulation, so our model consists of a system of coupled partial differential equations. To motivate our generalization of Eq. 1, we pay careful attention to the underlying biological features. This leads us to develop two different mathematical descriptions of cell migration with Fucci technology.

Fundamental Fucci model

In the most fundamental format, Fucci highlights a subpopulation of cells in the G1 phase as being red, and another subpopulation of cells in the S/G2/M phase as being green. Motivated by the ability to distinguish between these two phases of the cell cycle, we develop a mathematical model with two subpopulations: $v_r(x,t)$ and $v_g(x,t)$. Here, the $v_r(x,t)$ subpopulation corresponds to the red cells and the $v_g(x,t)$ subpopulation corresponds to the green cells. We refer to this model as the fundamental model.

Extended Fucci model

In some experimental descriptions, cell biologists identify an additional subpopulation that corresponds to the situation where both of the red and green probes are active simultaneously, giving rise to a third subpopulation that appears to be yellow. This overlap of the red and green fluorescence occurs during the early S, or eS, phase. Using experimental images, we find that the yellow subpopulation is more difficult to reliably identify than either the red or green subpopulations, as only a very small proportion of the cell population appear to be distinctly yellow. This is, in some sense, expected, because the yellow subpopulation results from the transient overlap of the G1 phase (red) and the S/G2/M phase (green). Despite this difficulty, we also develop another mathematical model which is capable of representing the three subpopulations: $u_r(x,t)$ is the red subpopulation, $u_y(x,t)$ is the yellow subpopulation, and $u_g(x,t)$ is the green subpopulation. We refer to this model as the extended model.

The fundamental and extended models are both related to the FKPP model with the dependent variable $s(x,t)$. To summarize the similarities and differences between the fundamental and extended models, the FKPP model, and the relationship between these mathematical models and

the underlying biology, we report the dependent variables and their biological interpretation in [Table 1](#).

In this work, we present information relating to both the fundamental and the extended models, but we focus on developing, to our knowledge, a new mathematical analysis of the fundamental FUCCI model. Furthermore, we quantitatively apply the fundamental model, to our knowledge, to new experimental data. There are two types of parameters in our model, namely transition rates between phases of the cell cycle, and diffusion coefficients describing the rate of cell migration. The transition rates between phases of the cell cycle are estimated using experimental data from Haass et al. (3), who report data relating to the time spent in each phase of the cell cycle. Using new experimental data in the form of images of scratch assays of FUCCI-transduced melanoma cells, we extract quantitative information about cell density as a function of position and time, and compare these quantitative data with the predictions of our fundamental model. Because this is, to our knowledge, the first time that a mathematical model has been used to predict a cell migration experiment with FUCCI-transduced cells, we focus on 2D cell migration experiments as this is the most common experimental platform because of convenience, simplicity, and low cost (28). 2D cell migration assays are valuable because they are often used as high-throughput screening tools in conjunction with more sophisticated preclinical models (28). In addition to showing how these mathematical models can be used to predict the 2D experiments, numerical solutions of the mathematical model show the formation of traveling wave solutions that are a combination of coupled wavefronts and pulses. We also derive an analytical expression for the minimum wave speed of the traveling waves, and we explore how these results are different from those of the standard FKPP equation, given in [Eq. 1](#).

This article is organized as follows. In the [Materials and Methods](#), we detail the experimental protocol used to perform the scratch assays using FUCCI-transduced melanoma cells. We also outline the numerical analysis of our mathematical models. In the [Results and Discussion](#), we present and discuss our mathematical models, and compare numerical solutions of the fundamental model with new data from scratch assays of melanoma cells. We then analyze our

models numerically for traveling wave solutions, and for the fundamental model we derive an analytical expression for the minimum wave speed.

MATERIALS AND METHODS

Experiments

Cell culture. The human melanoma cell lines C8161 (kindly provided by Mary Hendrix, Chicago, IL), 1205Lu and WM983C (both kindly provided by Meenhard Herlyn, Philadelphia, PA) were genotypically characterized (29–32), grown as described (33) (using 4% fetal bovine serum instead of 2%), and authenticated by STR fingerprinting (QIMR Berghofer Medical Research Institute, Herston, Australia).

Fluorescent ubiquitination-based cell cycle indicator. To generate stable melanoma cell lines expressing the FUCCI constructs, mKO2-hCdt1 (30–120) and mAG-hGem (1–110) (2) were subcloned into a replication-defective, self-inactivating lentiviral expression vector system as previously described (33). The lentivirus was produced by cotransfection of human embryonic kidney 293T cells. High-titer viral solutions for mKO2-hCdt1 (30:120) and mAG-hGem (1:110) were prepared and used for cotransduction into the melanoma cell lines, and subclones were generated by single cell sorting (3,5,34).

Wound healing migration assay. Experiments were performed using the three melanoma cell lines C8161, 1205Lu, and WM983C. For each cell line, three independent experiments were performed. FUCCI-transduced melanoma cells from each cell line were seeded in a six-well plate to subconfluence. The seeding density was adjusted according to the doubling time for the cell line. The monolayer was scraped with a p200 pipette tip, and images were taken at regular time intervals.

Mathematical model

Numerical solutions of [Eqs. 2, 3, 4, 5](#), and [6](#) are obtained on a domain, $0 \leq x \leq L$, with grid spacing Δx , and with uniform time steps of duration Δt . The details are in the [Supporting Material](#).

In this study, the initial condition takes one of three forms, depending on the purpose of the modeling exercise:

Modeling a scratch assay. The first set of modeling results involves using the fundamental mathematical model to mimic a set of experimental data from a scratch assay. For this purpose, we take images from the experiment, manually count numbers of cells in each phase of the cell cycle, and use these numbers to specify $v_r(x,0)$ and $v_g(x,0)$. To simulate the experiment, we solve the governing equation numerically on a finite domain, $0 \leq x \leq L$, where L is chosen to match the physical dimension of the experimental image.

Exploring the minimum wave speed of traveling wave solutions. The second set of modeling results involves studying long-time numerical solutions of the mathematical model to examine the possibility of traveling wave solutions. To ensure that we focus on the most biologically relevant traveling-

TABLE 1 Summary and Comparison of the Fundamental and Extended Models and the FKPP Model

Model	Equation Reference	Dependent Variables	Biological Interpretation
FKPP	Eq. 1	$s(x,t)$	total cell density is a function of position x and time t
Fundamental FUCCI	Eqs. 2 and 3	$v_r(x,t)$ $v_g(x,t)$	cell density for cells in G1 (red) phase is a function of position x and time t cell density for cells in S/G2/M (green) phase is a function of position x and time t
Extended FUCCI	Eqs. 4, 5, and 6	$s(x,t)$ $u_r(x,t)$ $u_y(x,t)$ $u_g(x,t)$ $s(x,t)$	total cell density, $s(x,t) = v_r(x,t) + v_g(x,t)$, is a function of position x and time t cell density for cells in G1 (red) phase is a function of position x and time t cell density for cells in eS (yellow) phase is a function of position x and time t cell density for cells in S/G2/M (green) phase is a function of position x and time t total cell density, $s(x,t) = u_r(x,t) + u_y(x,t) + u_g(x,t)$, is a function of position x and time t

wave solutions, we apply initial conditions with compact support. Further details are provided in the [Results and Discussion](#).

Dispersion relation. Having demonstrated the existence of traveling wave solutions, we then analyze how the long-time traveling wave speed depends on the decay rate of the initial condition for the fundamental model. Further details are provided in the [Results and Discussion](#).

RESULTS AND DISCUSSION

Experimental data

Our experimental data come from 2D scratch assays performed with Fucci-transduced melanoma cells. In particular, we use the C8161, 1205Lu and WM983C melanoma cell lines (3). Here we provide analysis for the C8161 and 1205Lu cell lines, which have very different cell cycle dynamics. We use these two cell lines to demonstrate that our model can predict the cell density for cell lines with a wide range of transition rates. The analysis for the WM983C cell line is in [Fig. S1](#). The WM983C cell line has cell cycle dynamics intermediate between the C8161 and 1205Lu cell lines.

In these experiments, melanoma cells migrate into a gap created by scratching the cell monolayer, and cell proliferation acts to increase the density of the monolayer. Still images of the scratch assays are obtained at four time points after the scratch is made: 0, 6, 12, and 18 h for the C8161 cell line, see [Fig. 1, A–D](#); 0, 16, 32, and 48 h for the 1205Lu cell line, see [Fig. 2, A–D](#); and 0, 16, 32, and 48 h for the WM983C cell line, see [Fig. S1, A–D](#). From these images, the nuclei of individual cells can be observed as red (G1 phase), yellow (eS phase) or green (S/G2/M phase). Over the time period of the experiments, the cells migrate into the gap, and cell proliferation is evident from the increasing density of cells behind the moving front. A notable feature of each of the images is that very few cells appear to be distinctly yellow. Almost all of the yellow cells appear to be either partly green and yellow, or partly red and yellow. This ambiguity motivates us to work with the fundamental mathematical model, which treats the yellow eS phase as part of the red G1 and green S/G2/M phases.

Although the images in [Figs. 1, A–D](#), [2, A–D](#), and [S1, A–D](#), provide some quantitative data about these particular scratch assays for these particular cell lines, the purpose of using a mathematical model is to provide significant generalizations beyond what is possible when working purely with experiments. For example, if we use this kind of data to parameterize a mathematical model, then we ought to be able to use the parameterized mathematical model to make predictions about varying different aspects of the experiment, such as changing the width of the scratch, the timescale of the experiment, or the initial density of the monolayer. To parameterize our mathematical model we require cell density data from the experiment. Although cells are free to move in two dimensions,

the geometry of the experiment is such that the cell density is spatially uniform in the vertical, y , direction. We therefore quantify the cell density as a function of horizontal position, x , at various times, t (35). Overall, this geometrical simplification allows us to describe the cell density data as a function of one spatial coordinate only, and we can therefore use a 1D mathematical model to describe this kind of data (35).

To obtain cell density data from the images in [Figs. 1, A–D](#), [2, A–D](#), and [S1, A–D](#), we divide each image into a series of vertical columns, each of width $50\ \mu\text{m}$. We manually count the number of cells of each color in each column. As previously discussed, there is some degree of ambiguity in classifying a cell as yellow, as almost all of the yellow cells appear to be a mixture of either red and yellow, or a mixture of green and yellow. This ambiguity is probably due to the fact that yellow arises from the transient overlap of red and green fluorescence. Consequently, we take the most straightforward approach and classify all of the cells as being either red or green. In this way we can work with just two subpopulations. Given the cell counts, we divide each cell count in each column by the area of that column to give the dimensional, column-averaged, cell density. These estimates of dimensional cell density are then converted into estimates of nondimensional cell density by dividing through by the carrying capacity density, K . These data are provided in the [Supporting Material](#). To estimate K (36), we assume that the cells are uniformly sized disks, and that the maximum monolayer density corresponds to hexagonal packing of cells. Hexagonal close packing corresponds to one cell at each vertex of the hexagon, and one cell at the center of the hexagon, meaning that the hexagon contains the equivalent of three cells. The area of the hexagon is $3\sqrt{3}R^2/2$, where R is the circumradius. If the radius of the cells is a then, because $R = 2a$, the carrying capacity is given by $K = 1/(2\sqrt{3}a^2)$. The cell diameter of C8161 melanoma cells is $\sim 17\ \mu\text{m}$ (37). So, with $a = 8.5\ \mu\text{m}$, we have $K = 0.004\ \text{cells}\ \mu\text{m}^{-2}$, to one significant figure. We use the same value of K for the 1205Lu and WM983C melanoma cells, as cells from the three cell lines are similar in size.

[Fig. 1, I–L](#) shows the resulting experimental cell density profiles for C8161 cells at 0, 6, 12 and 18 h, respectively. [Fig. 2, G–J](#) shows the resulting experimental cell density profiles for 1205Lu cells at 0, 16, 32 and 48 h, respectively. Similar profiles for the WM983C cells are in [Fig. S1, G–J](#). These figures provide quantitative information about how the population of cells migrates into the gap, while simultaneously proliferating to increase the density of the spreading monolayer, as we observed qualitatively in [Figs. 1, A–D](#), [2, A–D](#), and [S1, A–D](#). These cell density profiles, however, quantify the cell density of each subpopulation, and allow the changes in cell density over time to be determined quantitatively, which is not possible through visual interpretation of the images.

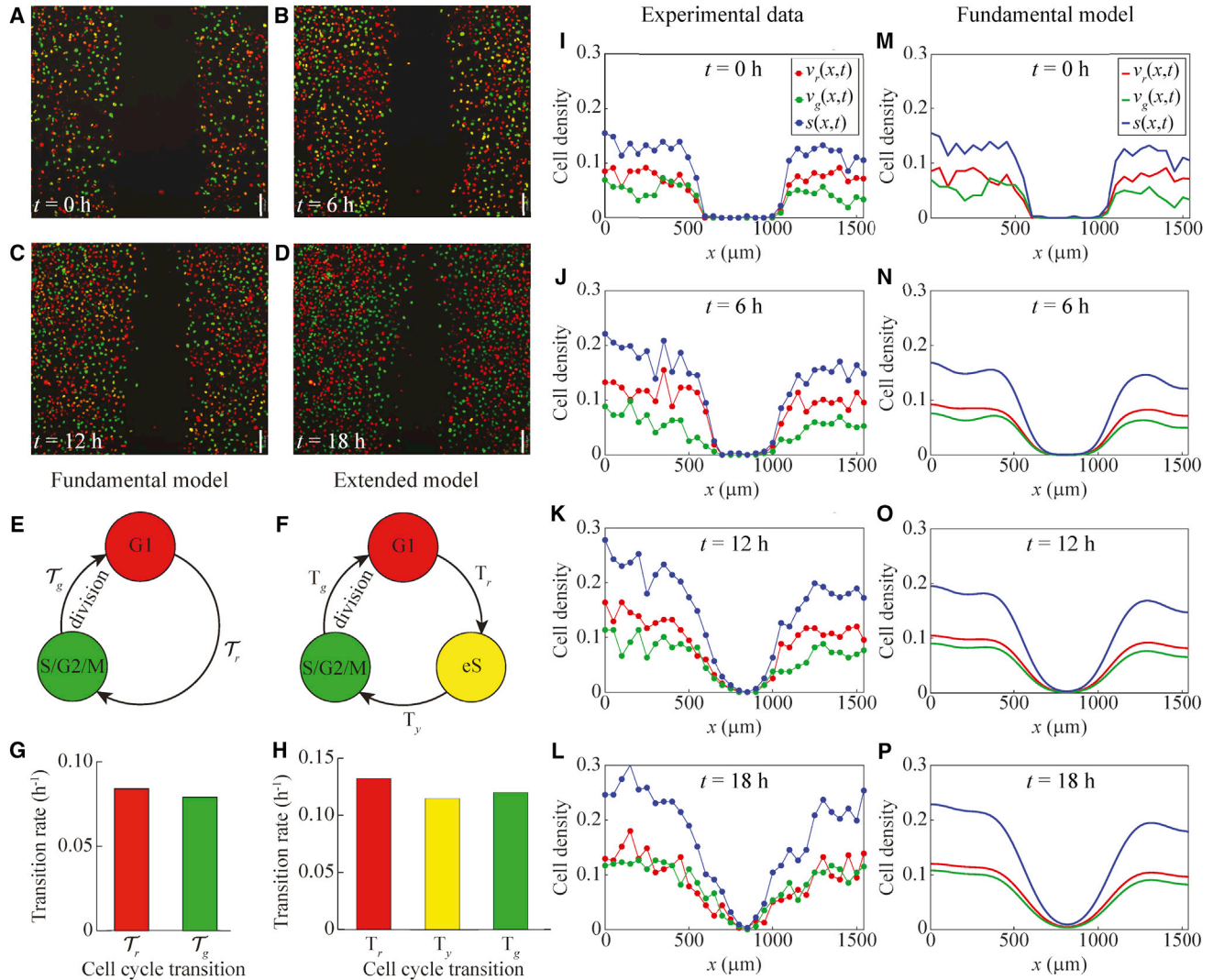


FIGURE 1 Comparison of experimental data and the fundamental model for a scratch assay of FUCCI-transduced C8161 melanoma cells. (A–D) Still images of a scratch assay with FUCCI-transduced C8161 melanoma cells at time 0 h, 6 h, 12 h and 18 h, respectively. Scale bar, 150 μm . (E) Schematic of the fundamental model with two subpopulations indicating the transitions between the cell cycle phases indicated by FUCCI. (F) Schematic of the extended model with three subpopulations indicating the transitions between the cell cycle phases indicated by FUCCI. (G) Estimated transition rates from one cell cycle phase to the next for the fundamental model with two subpopulations, based on data from the C8161 cell line from Figure 1C in (3). (H) Estimated transition rates from one cell cycle phase to the next for the extended model with three subpopulations, based on data from the C8161 cell line from Figure 1C in (3). (I–L) Experimental non-dimensional cell density data at 0 h, 6 h, 12 h and 18 h, respectively (based on images in (A)–(D)). The cell density is treated as a function of x and t only, owing to the fact that the initial density does not depend on the vertical coordinate, y . (M–P) Numerical solutions of the fundamental model (Eqs. 2 and 3), at 0 h, 6 h, 12 h and 18 h. The numerical solutions are obtained with $\Delta x = 0.1 \mu\text{m}$, $\Delta t = 0.1$ h, $L = 1542 \mu\text{m}$, diffusion coefficients $D_r = D_g = 400 \mu\text{m}^2 \text{h}^{-1}$, transition rates $\kappa_r = 0.084 \text{h}^{-1}$ and $\kappa_g = 0.079 \text{h}^{-1}$, and initial conditions are the same as for the experimental data. To see this figure in color, go online.

Movies of scratch assays associated with the three cell lines considered in this work are provided in the [Supporting Material](#).

Model development

We now describe the FUCCI scratch assays using the fundamental model. As previously explained, cells in the experiment move in two dimensions. However, the geom-

etry of the experiment means that the cell density is spatially uniform in the vertical, y , direction. Therefore, we can model the experiment with a 1D model, where the independent variables are time, t , and the horizontal coordinate, x (35).

As summarized in the [Introduction](#), in the FUCCI system, red and green fluorescent proteins are fused to different regulators of the cell cycle so that a cell in G1 phase fluoresces red, and a cell in S/G2/M phase fluoresces green. During the

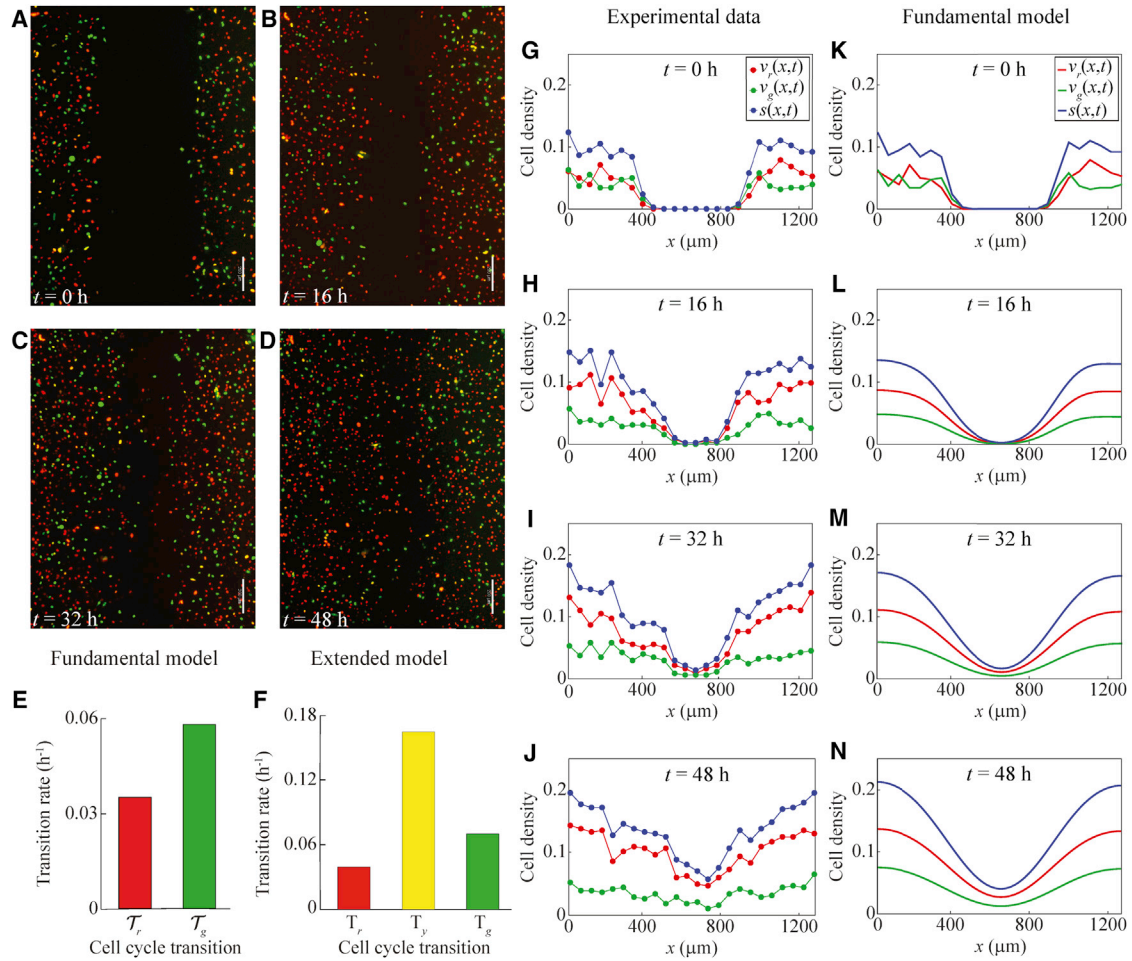


FIGURE 2 Comparison of experimental data and the fundamental model for a scratch assay of FUCCI-transduced 1205Lu melanoma cells. Comparison of experimental data and the fundamental model for a scratch assay of FUCCI-transduced 1205Lu melanoma cells. (A–D) Still images of a scratch assay with FUCCI-transduced 1205Lu melanoma cells at time 0 h, 16 h, 32 h and 48 h, respectively. Scale bar, 200 μm . (E) Estimated transition rates from one cell cycle phase to the next for the fundamental model with two subpopulations, based on data from the 1205Lu cell line from Figure 1C in (3). (F) Estimated transition rates from one cell cycle phase to the next for the extended model with three subpopulations, based on data from the 1205Lu cell line from Figure 1C in (3). (G–J) Experimental non-dimensional cell density data at 0 h, 16 h, 32 h and 48 h, respectively (based on images in (A)–(D)). The cell density is treated as a function of x and t only, owing to the fact that the initial density does not depend on the vertical coordinate, y . (K–N) Numerical solutions of the fundamental model (Eqs. 2 and 3), at 0 h, 16 h, 32 h and 48 h. The numerical solutions are obtained with $\Delta x = 0.1 \mu\text{m}$, $\Delta t = 0.1 \text{ h}$, $L = 1254 \mu\text{m}$, diffusion coefficients $\mathcal{D}_r = \mathcal{D}_g = 400 \mu\text{m}^2 \text{h}^{-1}$, transition rates $\kappa_r = 0.035 \text{ h}^{-1}$ and $\kappa_g = 0.058 \text{ h}^{-1}$, and initial conditions the same as for the experimental data. To see this figure in color, go online.

cell cycle transition from G1 phase to S phase, referred to as eS phase, the red FUCCI signal decreases and the green FUCCI signal increases, producing varying shades of yellow fluorescence, ranging from darker yellow to lighter yellow. The indication of the eS (yellow) phase is therefore secondary, as it arises from the overlap of red and green fluorescence. In the experimental images, it is difficult to identify the cells in eS phase as very few cells appear distinctly yellow, rather appearing shades of either red or green. For these reasons, our fundamental mathematical model is

$$\frac{\partial v_r}{\partial t} = \mathcal{D}_r \frac{\partial^2 v_r}{\partial x^2} - \kappa_r v_r + 2\kappa_g v_g(1-s), \quad (2)$$

$$\frac{\partial v_g}{\partial t} = \mathcal{D}_g \frac{\partial^2 v_g}{\partial x^2} - \kappa_g v_g(1-s) + \kappa_r v_r, \quad (3)$$

where $v_r(x,t)$ and $v_g(x,t)$ are the nondimensional cell densities of the coupled subpopulations corresponding to the G1 (red) and S/G2/M (green) phases of the cell cycle, respectively. The total density is $s(x,t) = v_r(x,t) + v_g(x,t)$. The rate at which cells in the G1 phase transition to the S/G2/M phase is κ_r , and the rate at which cells in the S/G2/M phase transition to the G1 phase is κ_g . The diffusion coefficients are \mathcal{D}_r for cells in phase G1, and \mathcal{D}_g for cells in phase S/G2/M. Although we are free to choose any realistic values for the diffusion coefficients, it is pertinent to set $\mathcal{D}_r = \mathcal{D}_g$, because

we are considering subpopulations of cells of the same type which differ only with respect to their cell cycle phase. Indeed, cells from various melanoma cell lines, including C8161, 1205Lu, and WM983C, appear to migrate independently of the cell cycle phases. For example, see the data in Figs. 6 and S3 in (3). We will employ this biologically motivated simplifying assumption at various points in our analysis. Note that in 2, the factor of two in the positive source term corresponds to a cell in phase S/G2/M undergoing division to produce two daughter cells in the phase G1, thereby doubling the local density.

Despite the challenges associated with the observation of the yellow eS phase, we also consider a mathematical model for three coupled subpopulations corresponding to G1, eS, and S/G2/M. We refer to this model as our extended model:

$$\frac{\partial u_r}{\partial t} = D_r \frac{\partial^2 u_r}{\partial x^2} - k_r u_r + 2k_g u_g (1 - s), \quad (4)$$

$$\frac{\partial u_y}{\partial t} = D_y \frac{\partial^2 u_y}{\partial x^2} - k_y u_y + k_r u_r, \quad (5)$$

$$\frac{\partial u_g}{\partial t} = D_g \frac{\partial^2 u_g}{\partial x^2} - k_g u_g (1 - s) + k_y u_y. \quad (6)$$

Here, $u_r(x,t)$, $u_y(x,t)$, and $u_g(x,t)$ are the nondimensional cell densities of the coupled subpopulations corresponding to the G1 (red), eS (yellow), and S/G2/M (green) phases of the cell cycle, respectively, with total cell density $s(x,t) = u_r(x,t) + u_y(x,t) + u_g(x,t)$. The G1 to eS transition rate is k_r , the eS to S/G2/M transition rate is k_y , and the S/G2/M to G1 transition rate is k_g . The diffusion coefficients are D_r for cells in phase G1, D_y for cells in phase eS, and D_g for cells in phase S/G2/M. Once again, we have no restriction on the choice of the values for the diffusion coefficients. The subpopulations consist of cells of the same type, they are only in different phases of the cell cycle. So, as discussed above for the fundamental model, the most obvious choice is to set $D_r = D_y = D_g$. As in Eq. 2, the factor of 2 in Eq. 4 corresponds to a cell in phase S/G2/M undergoing division to produce two daughter cells in the phase G1.

Model application

We illustrate our mathematical model in Figs. 1, 2, and S1, where we compare experimental data for scratch assays of Fucci-transduced melanoma cells with the fundamental model Eqs. 2 and 3. Fig. 1 corresponds to the C8161 melanoma cell line, Fig. 2 to the 1205Lu melanoma cell line, and Fig. S1 to the WM983C melanoma cell line.

Fig. 1 E describes, schematically, the fundamental model with two subpopulations, indicating the transitions between the cell cycle phases indicated by Fucci. We denote the transitions between the cell cycle phases as

$$\mathcal{T}_r : G_1 \xrightarrow{\kappa_r} S/G_2/M \quad \text{and} \quad \mathcal{T}_g : S/G_2/M \xrightarrow{\kappa_g} G_1, \quad (7)$$

where κ_r is the G1 to S/G2/M transition rate, and κ_g is the S/G2/M to G1 transition rate. Fig. 1 F is a similar schematic for the extended model with three subpopulations, where we denote the transitions between the cell cycle phases as

$$\begin{aligned} \mathcal{T}_r : G_1 &\xrightarrow{k_r} eS, \quad \mathcal{T}_y : eS \xrightarrow{k_y} S/G_2/M, \quad \text{and} \\ \mathcal{T}_g : S/G_2/M &\xrightarrow{k_g} G_1, \end{aligned} \quad (8)$$

where k_r , k_y , and k_g are the G1 to eS, eS to S/G2/M, and S/G2/M to G1 transition rates, respectively.

The estimated transition rates from one cell cycle phase to the next phase are based on Fucci data for the C8161, 1205Lu, and WM983C melanoma cell lines from Fig. 1 C in (3). These data report the duration of time spent in each cell cycle phase for at least 20 individual cells. To estimate the transition rate from one cell cycle phase to the next, we first calculate the arithmetic mean of the data in (3), giving the mean times: t_r for the G1 phase, t_y for the eS phase, and t_g for the S/G2/M phase. We then estimate the transition rates for the extended model as $k_r = (\ln 2)/t_r$ for the G1 to eS transition, $k_y = (\ln 2)/t_y$ for the eS to S/G2/M transition, and $k_g = (\ln 2)/t_g$ for the S/G2/M to G1 transition. The factor of $\ln 2$ arises because this data corresponds to cells in a low density environment, and so the cells are likely to be proliferating exponentially. To obtain estimates of the transition rates for the fundamental model, we assume that half of the time spent in the eS phase contributes to the time spent in the G1 phase, and the other half of the time spent in the eS phase contributes to the time spent in the S/G2/M phase. This means that we have $\kappa_r = (\ln 2)/(t_r + t_y/2)$ for the G1 to S/G2/M transition, and $\kappa_g = (\ln 2)/(t_g + t_y/2)$ for the S/G2/M to G1 transition. The estimated transition rates for the fundamental and extended models are shown in Fig. 1, G and H, respectively, for the C8161 cell line, in Fig. 2, E and F, respectively, for the 1205Lu cell line, and in Fig. S1, E and F, respectively, for the WM983C cell line. We can express the transition rates for the fundamental model in terms of those for the extended model as $\kappa_r = 2k_r k_y / (k_r + 2k_y)$ and $\kappa_g = 2k_g k_y / (k_g + 2k_y)$.

Previous studies examining the migration of various melanoma cell lines suggest that the diffusion coefficients lie within the range $100\text{--}500 \mu\text{m}^2 \text{h}^{-1}$ (38,39). Therefore, we will take an intermediate value and assume that the diffusivity of our melanoma cell lines is $\sim 400 \mu\text{m}^2 \text{h}^{-1}$.

For comparison with the experimental data for C8161 cells in Fig. 1, I–L, we show the numerical solutions of the fundamental model, Eqs. 2 and 3, in Fig. 1, M–P. Overall, the numerical solutions of Eqs. 2 and 3 in Fig. 1, M–P compare well with the corresponding experimental data in

Fig. 1, I–L. As time increases, the solution of the mathematical model shows the cell density profile spreading into the gap, and the cell density of each subpopulation increases throughout the domain due to proliferation. The relative size of each subpopulation also compares well between the numerical solutions and experimental data. Similarly, for comparison with the experimental data for 1205Lu cells in **Fig. 2, G–J**, we show the numerical solutions of the fundamental model, **Eqs. 2 and 3**, in **Fig. 2, K–N**. Once again, the numerical solutions of **Eqs. 2 and 3** in **Fig. 2, K–N** compare well with the corresponding experimental data in **Fig. 2, G–J**. A similar comparison for the WM983C cell line is in **Fig. S1**.

We note that other studies use partial differential equations to model scratch assays (16,19,35). None of these previous models, however, include the cell cycle phases of cells. Our results show potential for our model to successfully describe cell migration and proliferation along with cell cycle dynamics. With our model we can easily simulate experiments which would otherwise be expensive and time consuming. In particular, we can simulate experiments over longer periods of time, with different scratch widths, and with different parameters to accommodate different cell lines. Our model also provides quantitative data such as cell densities at any time and position within the domain.

Analysis

Numerical solutions

A key feature that can be observed in scratch assays initialized with a sufficiently wide scratch is the formation of a moving front of cells (16). This is important, because similar observations are relevant to malignant invasion and wound healing (16). The need to understand the key factors that drive moving fronts of cells, motivates an analysis of our models for scenarios in which a single front propagates along a wide domain.

We now simulate solutions of our models on a much wider domain using a different initial condition to examine the existence of traveling wave solutions. There are many

choices of initial condition; however, for the fundamental model, we set

$$v_r(x, 0) = v_g(x, 0) = \begin{cases} 0.5, & 0 \leq x < \xi, \\ 0, & \xi \leq x \leq L, \end{cases} \quad (9)$$

and for the extended model we set

$$\begin{aligned} u_r(x, 0) &= \begin{cases} 0.4, & 0 \leq x < \xi, \\ 0, & \xi \leq x \leq L, \end{cases} & u_y(x, 0) &= u_g(x, 0) \\ &= \begin{cases} 0.3, & 0 \leq x < \xi, \\ 0, & \xi \leq x \leq L, \end{cases} \end{aligned} \quad (10)$$

where the choice of the constant ξ is not critical. Because we use a numerical approach to explore traveling wave solutions, we set L to be sufficiently large so that the moving front does not interact with the boundary at $x = L$.

For this purpose, we obtain numerical solutions of the fundamental model, **Eqs. 2 and 3**, with typical solutions presented in **Fig. 3 A**. These results suggest that the solutions develop into an interesting traveling wave profile, where the density of cells in the G1 phase forms a moving pulse, whereas the density of cells in the S/G2/M phase forms a moving wavefront. Furthermore, the total cell density profile also moves as a wavefront profile. Analogous solutions of the extended model, **Eqs. 4, 5, and 6**, are shown in **Fig. 3 B**, which have similar features except that there is an additional pulse arising from cells in the eS phase. We find that the existence of these traveling waves is robust, and does not depend on the values of the diffusion coefficients. **Fig. S2** shows solutions of the fundamental model for $\mathcal{D}_g \neq \mathcal{D}_r$.

The appearance of traveling wave solutions that take the form of a wavefront is not unexpected, as the partial differential equations in our model are related to the FKPP equation, **Eq. 1**, which is well-known to exhibit traveling-wave solutions with a wavefront form (15,20). It is particularly interesting, however, that our model also exhibits traveling wave solutions with the form of a pulse, which are not observed for the FKPP equation. The pulses arise because only the cells near to the leading edge, where $s(x, t) < 1$,

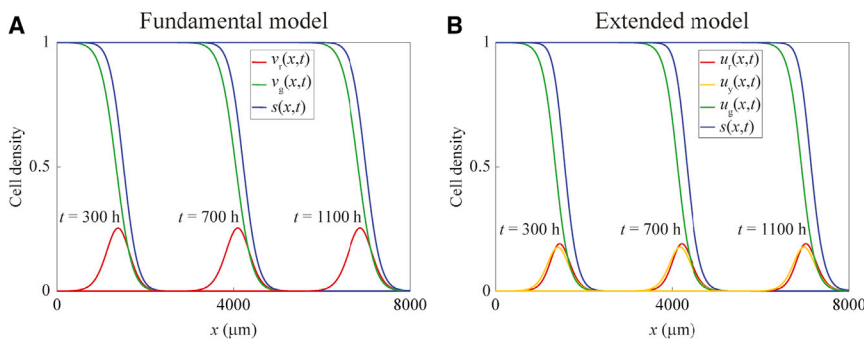


FIGURE 3 Numerical solutions demonstrating traveling wave behavior for the fundamental and extended models. (A) Numerical solutions of the fundamental model (**Eqs. 2 and 3**), obtained with $\Delta x = 1 \mu\text{m}$, $\Delta t = 1 \text{ h}$, $L = 8000 \mu\text{m}$, $D_r = D_g = 400 \mu\text{m}^2 \text{ h}^{-1}$, $K_r = K_g = 0.08 \text{ h}^{-1}$, and the initial condition given by **Eq. 9** with $\xi = 10$. (B) Numerical solutions of the extended model (**Eqs. 4 and 6**), obtained with $\Delta x = 1 \mu\text{m}$, $\Delta t = 1 \text{ h}$, $L = 8000 \mu\text{m}$, $D_r = D_y = D_g = 400 \mu\text{m}^2 \text{ h}^{-1}$, $k_r = k_y = k_g = 0.13 \text{ h}^{-1}$, and the initial condition given by **Eq. 10** with $\xi = 10$. To see this figure in color, go online.

have the opportunity to cycle from S/G2/M to G1, which involves cell division and can be inhibited by crowding effects. Behind the wavefront where $s(x,t)$ approaches unity, cells do not have enough space to divide, and so these cells remain in the S/G2/M phase.

Traveling wave analysis of the fundamental model

We now analyze the fundamental model, Eqs. 2 and 3, with the aim of understanding how the parameters in the model relate to the speed of the traveling wave solutions. To simplify our analysis, we nondimensionalize the problem by defining the new variables $t^* = \kappa_g t$ and $x^* = x\sqrt{\kappa_g/\mathcal{D}_r}$, and the parameters,

$$\mathcal{D} = \frac{\mathcal{D}_g}{\mathcal{D}_r} \quad \text{and} \quad \kappa = \frac{\kappa_r}{\kappa_g}, \quad (11)$$

to give the corresponding nondimensional model,

$$\frac{\partial v_r}{\partial t} = \frac{\partial^2 v_r}{\partial x^2} - \kappa v_r + 2v_g(1-s), \quad (12)$$

$$\frac{\partial v_g}{\partial t} = \mathcal{D} \frac{\partial^2 v_g}{\partial x^2} - v_g(1-s) + \kappa v_r, \quad (13)$$

in which the asterisks have been omitted for notational simplicity.

To examine the traveling wave solutions, we define the traveling wave coordinate, $z = x - ct$, where $c > 0$ is the wave speed associated with a traveling wave that propagates in the positive x direction. We seek solutions of Eqs. 12 and 13 of the form $v_r(x,t) = U(z)$ and $v_g(x,t) = V(z)$. Such solutions, if they exist, correspond to traveling wave solutions. Substituting $U(z)$ and $V(z)$ into Eqs. 12 and 13 gives the system of ordinary differential equations,

$$U'' + cU' - \kappa U + 2V(1 - U - V) = 0, \quad (14)$$

$$V'' + \frac{c}{\mathcal{D}}V' + \frac{\kappa}{\mathcal{D}}U - \frac{1}{\mathcal{D}}V(1 - U - V) = 0. \quad (15)$$

We want to find traveling-wave solutions that satisfy the conditions

$$U > 0, \quad \lim_{z \rightarrow -\infty} U(z) = 0 \quad \text{and} \quad \lim_{z \rightarrow \infty} U(z) = 0, \quad (16)$$

$$V > 0, \quad \lim_{z \rightarrow -\infty} V(z) = 1 \quad \text{and} \quad \lim_{z \rightarrow \infty} V(z) = 0. \quad (17)$$

Letting $W = U'$ and $X = V'$, we can write Eqs. 14 and 15 as a system of first-order equations:

$$U' = W, \quad (18)$$

$$V' = X, \quad (19)$$

$$W' = -cW + \kappa U - 2V(1 - U - V), \quad (20)$$

$$X' = -\frac{c}{\mathcal{D}}X - \frac{\kappa}{\mathcal{D}}U + \frac{1}{\mathcal{D}}V(1 - U - V). \quad (21)$$

The equilibrium points of Eqs. 18, 19, 20, and 21 are $(0, 0, 0, 0)$ and $(0, 1, 0, 0)$. Of all the solutions to Eqs. 18, 19, 20, and 21 in the 4D phase space, (U, V, W, X) , we seek a heteroclinic orbit from $(0, 1, 0, 0)$ to $(0, 0, 0, 0)$, which has the physically relevant property that $U > 0$ and $V > 0$.

The Jacobian of Eqs. 18, 19, 20, and 21 evaluated at $(0, 0, 0, 0)$ is

$$\begin{bmatrix} 0 & 0 & 1 & 0 \\ 0 & 0 & 0 & 1 \\ \kappa & -2 & -c & 0 \\ -\kappa/\mathcal{D} & 1/\mathcal{D} & 0 & -c/\mathcal{D} \end{bmatrix}. \quad (22)$$

The eigenvalues of Eq. 22 are the solutions of the corresponding characteristic equation

$$\mathcal{D}\lambda^4 + c(\mathcal{D} + 1)\lambda^3 + (c^2 - 1 - \mathcal{D}\kappa)\lambda^2 - c(1 + \kappa)\lambda - \kappa = 0. \quad (23)$$

To establish a condition for physically relevant traveling-wave solutions, where $U > 0$ and $V > 0$, we examine whether the solutions of Eq. 23 are either complex or real. The analytical solutions of this quartic equation (40) are quite complicated when $\mathcal{D} \neq 1$. Because we are considering subpopulations of the same cell type which differ only with respect to cell cycle phase, the biologically relevant case is when the two diffusion coefficients are equal, leading to $\mathcal{D} = 1$. In this case, by defining

$$\alpha^\pm(\kappa, c) = 2\kappa + c^2 + 2 \pm 2\sqrt{\kappa^2 + 6\kappa + 1}, \quad (24)$$

we can express the solutions of the quartic simply as

$$\begin{aligned} \lambda_1^\pm &= -\frac{1}{2}c \pm \frac{1}{2}\sqrt{\alpha^-(\kappa, c)} \quad \text{and} \\ \lambda_2^\pm &= -\frac{1}{2}c \pm \frac{1}{2}\sqrt{\alpha^+(\kappa, c)}. \end{aligned} \quad (25)$$

The eigenvalues λ_2^+ and λ_1^- are always real, and λ_1^+ and λ_2^- are real when $\alpha^-(\kappa, c) \geq 0$. If $\alpha^-(\kappa, c) < 0$, however, then λ_1^+ and λ_2^- are complex eigenvalues which yield solutions with oscillatory behavior, which necessarily involves negative cell densities. Because we are interested in traveling wave solutions for which U and V remain positive, we shall therefore require that $\alpha^-(\kappa, c) \geq 0$. It is then reasonable to suspect that, for a given $\kappa \geq 0$, the value of c such that $\alpha^-(\kappa, c) \geq 0$ is the minimum wave speed for the traveling waves, which we denote as

$$c_{\min}(\kappa) = \sqrt{-2\kappa - 2 + 2\sqrt{\kappa^2 + 6\kappa + 1}}. \quad (26)$$

The minimum wave speed is bounded above, and in fact $c_{\min}(\kappa) \rightarrow 2^-$ as $\kappa \rightarrow \infty$.

Equation 26 shows that the minimum speed of the traveling wave solution depends on κ , which is the ratio of the time the cells spend in phase S/G2/M to the time the cells spend in phase G1. In other words, the minimum wave speed depends on the cell cycle dynamics of the particular cells under consideration. We observe here that $\alpha^-(\kappa, c) \geq 0$ is a necessary condition for the existence of traveling waves. We have not demonstrated, however, that this condition is sufficient for the existence of traveling waves. This would require a formal proof of existence for the traveling waves, which is beyond the scope of this work.

Observe that if $\kappa > 0$ and $c \geq c_{\min}$ then λ^+_1, λ^-_1 , and λ^-_2 are real and negative, and λ^+_2 is real and positive. Therefore, the equilibrium point $(0, 0, 0, 0)$ is hyperbolic and has a 3D stable manifold and a 1D unstable manifold. The presence of a stable manifold at the point $(0, 0, 0, 0)$ is necessary for the existence of a heteroclinic orbit and the real eigenvalues allow for this orbit to correspond to physically relevant traveling wave solutions with $U > 0, V > 0$. This analysis does not constitute a formal proof of existence for the traveling waves, however it does show that our observations are consistent with their existence.

The Jacobian of the system Eqs. 18, 19, 20, and 21 evaluated at $(0, 1, 0, 0)$ is

$$\begin{bmatrix} 0 & 0 & 1 & 0 \\ 0 & 0 & 0 & 1 \\ \kappa + 2 & 2 & -c & 0 \\ -(\kappa + 1)/\mathcal{D} & -1/\mathcal{D} & 0 & -c/\mathcal{D} \end{bmatrix}. \quad (27)$$

The eigenvalues of Eq. 27 are the solutions of the corresponding characteristic equation

$$\mathcal{D}\lambda^4 + c(\mathcal{D} + 1)\lambda^3 + (c^2 + 1 - \mathcal{D}\kappa - 2\mathcal{D})\lambda^2 - c(1 + \kappa)\lambda + \kappa = 0. \quad (28)$$

Once again, the analytical solutions of this quartic equation (40) are quite complicated when $\mathcal{D} \neq 1$. For the biologically relevant case $\mathcal{D} = 1$, however, the solutions are

$$\begin{aligned} \lambda_3^\pm &= \frac{1}{2} \left(-c \pm \sqrt{c^2 + 4} \right) \quad \text{and} \\ \lambda_4^\pm &= \frac{1}{2} \left(-c \pm \sqrt{c^2 + 4\kappa} \right). \end{aligned} \quad (29)$$

If $\kappa > 0$, then λ^-_3 and λ^-_4 are real and negative, and λ^+_3 and λ^+_4 are real and positive. Therefore, the equilibrium point $(0, 1, 0, 0)$ is hyperbolic and has a 2D stable manifold and a 2D unstable manifold. The existence of an unstable manifold at the point is necessary for the presence of a traveling wave solution.

Fig. 4 A compares $c_{\min}(\kappa)$ in Eq. 26 with the wave speed estimates obtained from the numerical solutions of the partial differential equations (21). The numerical solutions are obtained using initial conditions with compact support, so we would expect the resulting traveling waves to have the minimum wave speed (15). We observe that the numerically estimated wave speed is consistent with Eq. 26 over the range of κ we consider. Therefore, we have numerical evidence to strongly support the claim that the minimum speed is given by Eq. 26.

In Fig. 4 B we show the asymptotic expansions of Eq. 26 as $\kappa \rightarrow 0$ and $\kappa \rightarrow \infty$:

$$c_{\min}(\kappa) = 2\kappa^{\frac{1}{2}} - 2\kappa^{\frac{3}{2}} + 5\kappa^{\frac{5}{2}} + O(\kappa^{\frac{7}{2}}) \text{ as } \kappa \rightarrow 0, \quad (30)$$

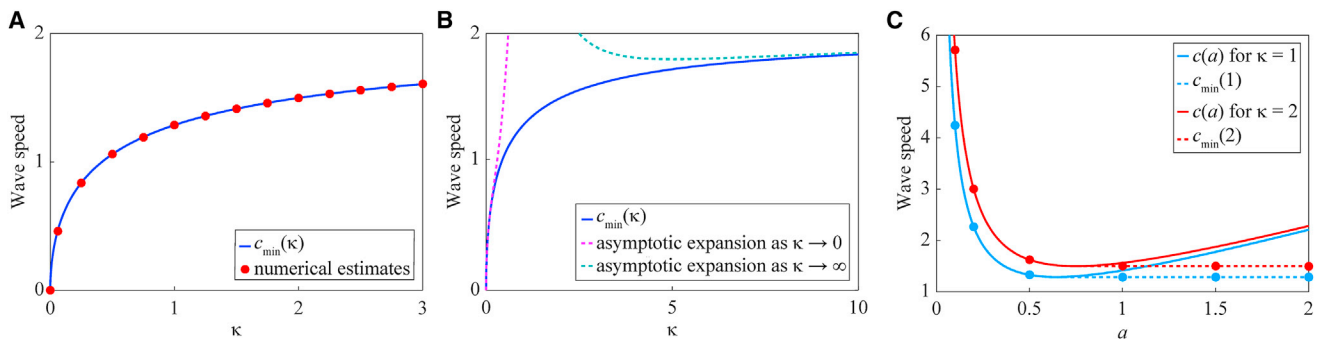


FIGURE 4 Minimum wave speed and the dispersion relation. (A) Comparison of $c_{\min}(\kappa)$ from Eq. 26 with the numerically-estimated wave speed for $s(x, t) = v_r(x, t) + v_g(x, t)$. Numerical solutions of Eqs. 12 and 13 are obtained with $\Delta x = 0.1, \Delta t = 0.001$ and $\mathcal{D} = 1$. Further, the initial condition is Eq. 9 with $\zeta = 10$. For $\kappa = 0$, there is no traveling wave, so we set $c = 0$. The numerical solutions are considered beginning with $\kappa = 0.06$, and then with increasing values of κ from 0.25 to 3, with increments of 0.25. From these numerical solutions we estimate the wave speed for $s(x, t) = v_r(x, t) + v_g(x, t)$ by using linear interpolation to find the position corresponding to $s(x, t) = 0.5$ on the wave for various times (21). (B) Asymptotic expansions for $c_{\min}(\kappa)$ as $\kappa \rightarrow 0$ and $\kappa \rightarrow \infty$. (C) Comparison of c from Eq. 35 with the wave speed estimated using numerical solutions and with c_{\min} from Eq. 26. Solutions are given for $\kappa = 1$ (blue) and $\kappa = 2$ (red). The continuous curves show c from Eq. 35. The dots represent the wave speed from numerical solutions obtained with $\Delta x = 0.1, \Delta t = 0.001, \mathcal{D} = 1$, and initial conditions of the form Eq. 36 with $\alpha = 0.1, 0.2, 0.5, 1, 1.5$ and 2. The dotted horizontal lines show c_{\min} from Eq. 26. To see this figure in color, go online.

$$c_{\min}(\kappa) = 2 - \frac{2}{\kappa} + \frac{5}{\kappa^2} + O\left(\frac{1}{\kappa^3}\right) \text{ as } \kappa \rightarrow \infty. \quad (31)$$

Thus, $c_{\min}(\kappa)$ behaves like $2\kappa^{1/2}$ when κ is small and like $2 - 2/\kappa$ when κ is large. We discuss the connection with the FKPP equation in the [Conclusions](#).

Dispersion relation

Here we investigate the relationship between the initial conditions for [Eqs. 12 and 13](#) with $\mathcal{D} = 1$, and the speed of the resulting traveling wave solution. Our approach is to examine the leading edge of the traveling wave, assuming that the initial conditions at infinity have an exponential form [\(15\)](#).

At the leading edge of the evolving waves, $s(x, t) = v_r(x, t) + v_g(x, t) \ll 1$, so we can linearize [Eqs. 12 and 13](#) to give

$$\frac{\partial \tilde{v}_r}{\partial t} = \frac{\partial^2 \tilde{v}_r}{\partial x^2} - \kappa \tilde{v}_r + 2\tilde{v}_g, \quad (32)$$

$$\frac{\partial \tilde{v}_g}{\partial t} = \frac{\partial^2 \tilde{v}_g}{\partial x^2} - \tilde{v}_g + \kappa \tilde{v}_r. \quad (33)$$

Assuming initial conditions of the form $\tilde{v}_r(x, 0) \sim Ae^{-ax}$ and $\tilde{v}_g(x, 0) \sim Be^{-bx}$ as $x \rightarrow \infty$ for arbitrary positive constants a , b , A , and B , we seek traveling wave solutions satisfying [Eqs. 32 and 33](#) of the form

$$\tilde{v}_r(x, t) = Ae^{-a(x-ct)} \quad \text{and} \quad \tilde{v}_g(x, t) = Be^{-b(x-ct)}, \quad (34)$$

corresponding to the leading edges of the pulse and wavefront solutions, respectively. Substituting [Eq. 34](#) into [Eqs. 32, 33, and 34](#) and solving for c gives

$$c = a - \frac{1}{a} + \frac{1}{2a} \left(1 - \kappa + \sqrt{\kappa^2 + 6\kappa + 1} \right). \quad (35)$$

The dispersion relation, [Eq. 35](#), depends only on a and κ , so we can obtain the traveling wave solutions with the form [Eq. 34](#) from initial conditions of the form

$$v_r(x, 0) = 0 \quad \text{and} \quad v_g(x, 0) = \begin{cases} 1, & 0 \leq x < \xi, \\ e^{-a(x-\xi)}, & \xi \leq x \leq L, \end{cases} \quad (36)$$

for constants ξ and $a > 0$. Note that for large a , this initial condition for v_g is approximately a Heaviside function. For a given κ , we observe that the minimum wave speed according to the dispersion relation, [Eq. 35](#), is equal to the minimum wave speed c_{\min} , given by [Eq. 26](#).

In [Fig. 4 C](#) we compare c from [Eq. 35](#) with estimates of the wave speed from numerical solutions of the governing partial differential equations, and with c_{\min} from [Eq. 26](#). The value of c given by the dispersion relation tends to infinity as both $a \rightarrow 0$ and $a \rightarrow \infty$, and has a unique min-

imum value for a given κ . The dispersion relation for the FKPP equation has similar properties [\(15\)](#). For a given κ , the numerical estimates of the wave speed agree with [Eq. 35](#) for increasing values of $a > 0$, until the minimum wave speed is obtained. As we further increase a , the numerical estimates of the wave speed remain constant, at the minimum value of the wave speed. Once again, the dispersion relation for the FKPP equation has similar properties [\(15\)](#).

CONCLUSIONS

Here we present, to our knowledge, the first mathematical model of cell migration that can be used to quantitatively describe experiments using Fucci technology, which highlights the spatial and temporal distribution of individual cells in different parts of the cell cycle. The fundamental model consists of two coupled partial differential equations, each of which governs the subpopulations of cells corresponding to the two phases of the cell cycle that are directly labeled by Fucci. Our study suggests that the model can describe cell migration and cell proliferation in a way that highlights the spatial and temporal distribution of two subpopulations. In particular, we show that the model can describe the dynamics of scratch assays performed with cells highlighted by Fucci. This is a useful outcome, as scratch assays are routinely employed to study cell migration, for example in the context of malignant invasion [\(35\)](#) and wound healing [\(16\)](#). Although a typical scratch assay may require several days to grow cells, and to perform and record the experiment, our model can simulate such an experiment on a single desktop computer in a few seconds. In addition, we can easily vary the parameters in our model to simulate experiments over any period of time, any scratch width, any geometry, and any cell line, provided that we have some information about the amount of time that is spent in each phase of the cell cycle. Therefore, this kind of computational modeling tool can provide valuable information to assist in the design and interpretation of these kinds of experiments conducted with Fucci.

In this work, we use numerical results to demonstrate the existence of traveling wave solutions. Furthermore, our analysis shows that the minimum wave speed depends on the ratio of the time spent in each of the G1 and S/G2/M phases. Another outcome of this study is that we derive an analytical expression for the minimum wave speed as a function of this ratio which, in dimensional variables, can be written as

$$c_{\min} = \sqrt{2\mathcal{D}_r \left(-\kappa_r - \kappa_g + \sqrt{\kappa_r^2 + 6\kappa_r\kappa_g + \kappa_g^2} \right)}. \quad (37)$$

This relationship is based on the biologically reasonable assumption that $\mathcal{D}_r = \mathcal{D}_g$, where \mathcal{D}_r is the diffusion

coefficient for cells in phase G1 and \mathcal{D}_g is the diffusion coefficient for cells in phase S/G2/M. Further, κ_r is the transition rate from G1 to S/G2/M and κ_g is the transition rate from S/G2/M to G1. It then follows from Eqs. 30 and 31 that $c_{\min} \sim 2\sqrt{\kappa_r \mathcal{D}_r}(1 - \kappa_r/\kappa_g)$ as $\kappa_r/\kappa_g \rightarrow 0$, and $c_{\min} \sim 2\sqrt{\kappa_g \mathcal{D}_g}(1 - \kappa_g/\kappa_r)$ as $\kappa_g/\kappa_r \rightarrow 0$. Therefore, when $\kappa_r/\kappa_g \ll 1$, so that cells spend much more time in phase G1 compared with phase S/G2/M, the minimum wave speed obtained from our fundamental FUCCI model, Eqs. 2 and 3, approaches the minimum wave speed obtained from the FKPP equation, Eq. 1. A similar observation holds for the case $\kappa_g/\kappa_r \ll 1$, corresponding to the situation where the cells spend much more time in phase S/G2/M compared with phase G1.

Traveling wave solutions are of great practical interest as cell migration tends to exhibit traveling wave characteristics (16). The analytical expression we derive for the minimum wave speed is of practical interest, as a moving front of cells can be thought of as acting like a traveling wave solution, so our expression can provide a prediction for the speed of the moving front in experimental studies. The traveling wave solutions of the fundamental model are mathematically interesting because they are a combination of moving wavefronts and moving pulses. Monotonically decreasing wavefront solutions are well known for the FKPP equation, and because our models are related to the FKPP equation, it is not surprising that wavefront solutions are also observed in our study. It is interesting, however, that traveling wave solutions of our models involve pulses, which are not features of the traveling wave solutions of the FKPP equation.

There are many possibilities for future work arising from this study. An area of particular interest would involve using our models to quantitatively study how the migration of melanoma cells and the cell cycle for melanoma cells are affected by the application of particular melanoma drugs. Indeed, there is still much to learn regarding the effects of introduced drugs on melanoma cell activity (3). These kinds of drugs often act to arrest the cell cycle, thereby preventing melanoma proliferation. Another feature that could be examined is the role of contact inhibition and cell cycle arrest, because it is accepted that cells in relatively high-density environments can undergo cell cycle arrest. Indeed, our model does not account for this phenomenon, because we are interested in low to moderate cell densities. Another way that this study could be extended is to consider additional phases of the cell cycle. This is of interest because a very recent extension of FUCCI technology, referred to as FUCCI4 (41), highlights all four cell cycle phases G1, S, G2, and M. If extended to four coupled partial differential equations, our modeling framework could be used to quantitatively describe cell migration where individual cells are highlighted using FUCCI4.

SUPPORTING MATERIAL

Supporting Materials and Methods, two figures, one table, and three movies are available at [http://www.biophysj.org/biophysj/supplemental/S0006-3495\(18\)30062-6](http://www.biophysj.org/biophysj/supplemental/S0006-3495(18)30062-6).

ACKNOWLEDGMENTS

We thank Emeritus Professor Sean McElwain and two anonymous referees for helpful comments.

N.K.H. is a Cameron fellow of the Melanoma and Skin Cancer Research Institute, Australia, and is supported by the National Health and Medical Research Council (AP1084893). M.J.S. is an Australian Research Council Future Fellow, and is supported by the Australian Research Council Discovery Program (DP170100474). S.W.M. is supported by the Australian Research Council Discovery Program (DP140100249).

REFERENCES

1. Alberts, B., A. Johnson, ..., P. Walter. 2014. *Molecular Biology of the Cell*, 6th. Taylor & Francis, Hamden, CT.
2. Sakaue-Sawano, A., H. Kurokawa, ..., A. Miyawaki. 2008. Visualizing spatiotemporal dynamics of multicellular cell-cycle progression. *Cell*. 132:487–498.
3. Haass, N. K., K. A. Beaumont, ..., W. Weninger. 2014. Real-time cell cycle imaging during melanoma growth, invasion, and drug response. *Pigment Cell Melanoma Res.* 27:764–776.
4. Shand, F. H. W., S. Ueha, ..., K. Matsushima. 2014. Tracking of inter-tissue migration reveals the origins of tumor-infiltrating monocytes. *Proc. Natl. Acad. Sci. USA*. 111:7771–7776.
5. Beaumont, K. A., A. Anfosso, ..., N. K. Haass. 2015. Imaging- and flow cytometry-based analysis of cell position and the cell cycle in 3D melanoma spheroids. *J. Vis. Exp.* 106:e53486.
6. Beaumont, K. A., D. S. Hill, ..., N. K. Haass. 2016. Cell cycle phase-specific drug resistance as an escape mechanism of melanoma cells. *J. Invest. Dermatol.* 136:1479–1489.
7. Dowling, M. R., A. Kan, ..., P. D. Hodgkin. 2014. Stretched cell cycle model for proliferating lymphocytes. *Proc. Natl. Acad. Sci. USA*. 111:6377–6382.
8. Sandler, O., S. P. Mizrahi, ..., N. Q. Balaban. 2015. Lineage correlations of single cell division time as a probe of cell-cycle dynamics. *Nature*. 519:468–471.
9. Pauklin, S., and L. Vallier. 2013. The cell-cycle state of stem cells determines cell fate propensity. *Cell*. 155:135–147.
10. Rocco, M., D. Schmitter, ..., M. P. Lutolf. 2013. Predicting stem cell fate changes by differential cell cycle progression patterns. *Development*. 140:459–470.
11. Sadeghi, H. M., B. Seitz, ..., P. J. McDonnell. 1998. In vitro effects of mitomycin-C on human keratocytes. *J. Refract. Surg.* 14:534–540.
12. Simpson, M. J., K. K. Treloar, ..., R. E. Baker. 2013. Quantifying the roles of cell motility and cell proliferation in a circular barrier assay. *J. R. Soc. Interface*. 10:20130007.
13. Holmes, W. R., M. A. Mata, and L. Edelstein-Keshet. 2015. Local perturbation analysis: a computational tool for biophysical reaction-diffusion models. *Biophys. J.* 108:230–236.
14. Fisher, R. A. 1937. The wave of advance of advantageous genes. *Ann. Eugen.* 7:355–369.
15. Murray, J. D. 2002. *Mathematical Biology: 1. An Introduction*, 3rd. Springer, New York, New York.
16. Maini, P., D. L. S. McElwain, and D. Leavesley. 2004. Travelling waves in a wound healing assay. *Appl. Math. Lett.* 17:575–580.

17. Johnston, S. T., E. T. Shah, ..., M. J. Simpson. 2015. Estimating cell diffusivity and cell proliferation rate by interpreting IncuCyte ZOOM assay data using the Fisher-Kolmogorov model. *BMC Syst. Biol.* 9:38.
18. Sengers, B. G., C. P. Please, and R. O. Oreffo. 2007. Experimental characterization and computational modelling of two-dimensional cell spreading for skeletal regeneration. *J. R. Soc. Interface.* 4:1107–1117.
19. Landman, K. A., A. Q. Cai, and B. D. Hughes. 2007. Travelling waves of attached and detached cells in a wound-healing cell migration assay. *Bull. Math. Biol.* 69:2119–2138.
20. Canosa, J. 1973. On a nonlinear diffusion equation describing population growth. *IBM J. Res. Develop.* 17:307–313.
21. Simpson, M. J., and K. A. Landman. 2006. Characterizing and minimizing the operator split error for Fishers equation. *Appl. Math. Lett.* 19:604–612.
22. Marel, A.-K., M. Zorn, ..., J. O. Rädler. 2014. Flow and diffusion in channel-guided cell migration. *Biophys. J.* 107:1054–1064.
23. Holder, A. B., M. R. Rodrigo, and M. A. Herrero. 2014. A model for acid-mediated tumour growth with nonlinear acid production term. *Appl. Math. Comput.* 227:176–198.
24. Kimpson, L. S., J. P. Whiteley, ..., J. M. Oliver. 2013. Multiple travelling-wave solutions in a minimal model for cell motility. *Math. Med. Biol.* 30:241–272.
25. Marchant, B. P., J. Norbury, and H. M. Byrne. 2006. Biphasic behaviour in malignant invasion. *Math. Med. Biol.* 23:173–196.
26. Curtis, C. W., and D. M. Bortz. 2012. Propagation of fronts in the Fisher-Kolmogorov equation with spatially varying diffusion. *Phys. Rev. E Stat. Nonlin. Soft Matter Phys.* 86:066108.
27. Denman, P. K., D. L. S. McElwain, and J. Norbury. 2007. Analysis of travelling waves associated with the modelling of aerosolised skin grafts. *Bull. Math. Biol.* 69:495–523.
28. Beaumont, K. A., N. Mohana-Kumaran, and N. K. Haass. 2013. Modeling melanoma in vitro and in vivo. *Healthcare (Basel)*. 2:27–46.
29. Davies, M. A., K. Stemke-Hale, ..., J. E. Gershenwald. 2009. Integrated molecular and clinical analysis of AKT activation in metastatic melanoma. *Clin. Cancer Res.* 15:7538–7546.
30. Hoek, K. S., N. C. Schlegel, ..., R. Dummer. 2006. Metastatic potential of melanomas defined by specific gene expression profiles with no BRAF signature. *Pigment Cell Res.* 19:290–302.
31. Smalley, K. S., R. Contractor, ..., M. Herlyn. 2007. An organometallic protein kinase inhibitor pharmacologically activates p53 and induces apoptosis in human melanoma cells. *Cancer Res.* 67:209–217.
32. Smalley, K. S. M., R. Contractor, ..., M. Herlyn. 2007. Ki67 expression levels are a better marker of reduced melanoma growth following MEK inhibitor treatment than phospho-ERK levels. *Br. J. Cancer.* 96:445–449.
33. Smalley, K. S., P. Brafford, ..., M. Herlyn. 2005. Up-regulated expression of *Zonula occludens* protein-1 in human melanoma associates with N-cadherin and contributes to invasion and adhesion. *Am. J. Pathol.* 166:1541–1554.
34. Spoerri, L., K. A. Beaumont, ..., N. K. Haass. 2017. Real-time cell cycle imaging in a 3D cell culture model of melanoma. *Methods Mol. Biol.* 1612:401–416.
35. Jin, W., E. T. Shah, ..., M. J. Simpson. 2016. Reproducibility of scratch assays is affected by the initial degree of confluence: experiments, modelling and model selection. *J. Theor. Biol.* 390:136–145.
36. Warne, D. J., R. E. Baker, and M. J. Simpson. 2017. Optimal quantification of contact inhibition in cell populations. *Biophys. J.* 113:1920–1924.
37. Yohem, K. H., D. J. Slymen, ..., F. L. Meyskens, Jr. 1988. Radiation survival of murine and human melanoma cells utilizing two assay systems: monolayer and soft agar. *Br. J. Cancer.* 57:64–69.
38. Treloar, K. K., M. J. Simpson, ..., R. E. Baker. 2013. Multiple types of data are required to identify the mechanisms influencing the spatial expansion of melanoma cell colonies. *BMC Syst. Biol.* 7:137.
39. Haridas, P., C. J. Penington, ..., M. J. Simpson. 2017. Quantifying rates of cell migration and cell proliferation in co-culture barrier assays reveals how skin and melanoma cells interact during melanoma spreading and invasion. *J. Theor. Biol.* 423:13–25.
40. Abramowitz, M., and I. A. Stegun. 1964. Handbook of Mathematical Functions with Formulas, Graphs, and Mathematical Tables. United States Department of Commerce, National Bureau of Standards (NBS), Washington, DC.
41. Bajar, B. T., A. J. Lam, ..., M. Z. Lin. 2016. Fluorescent indicators for simultaneous reporting of all four cell cycle phases. *Nat. Methods.* 13:993–996.

Biophysical Journal, Volume 114

Supplemental Information

Mathematical Models for Cell Migration with Real-Time Cell Cycle Dynamics

Sean T. Vittadello, Scott W. McCue, Gency Gunasingh, Nikolas K. Haass, and Matthew J. Simpson

Contents

1	Numerical solutions of the mathematical model	2
2	Scratch assay of FUCCI-transduced WM983C melanoma cells	3
3	Numerical solutions demonstrating travelling wave behaviour	5
	References	6

1 Numerical solutions of the mathematical model

The numerical solutions of Eqs (2)–(3) and Eqs (4)–(6) are obtained using an implicit finite difference approximation. In particular, we use a central difference approximation for the spatial derivative term, and a backward Euler approximation for the temporal derivative [1]. The spatial domain, $0 \leq x \leq L$, is uniformly discretised with grid spacing Δx . No-flux boundary conditions are implemented at both $x = 0$ and $x = L$. The temporal domain is uniformly discretised with time steps of duration Δt . The resulting non-linear system of equations is solved using the Thomas algorithm [1], applying Picard iteration at each time step until the maximum absolute change in the given dependent variable across the spatial grid is less than a specified tolerance, ϵ .

2 Comparison of experimental data and the fundamental model for a scratch assay of FUCCI-transduced WM983C melanoma cells.

In Fig S1 we present experimental data for the WM983C melanoma cell line, together with corresponding numerical solutions of the fundamental model. The numerical solutions compare well with the experimental data.

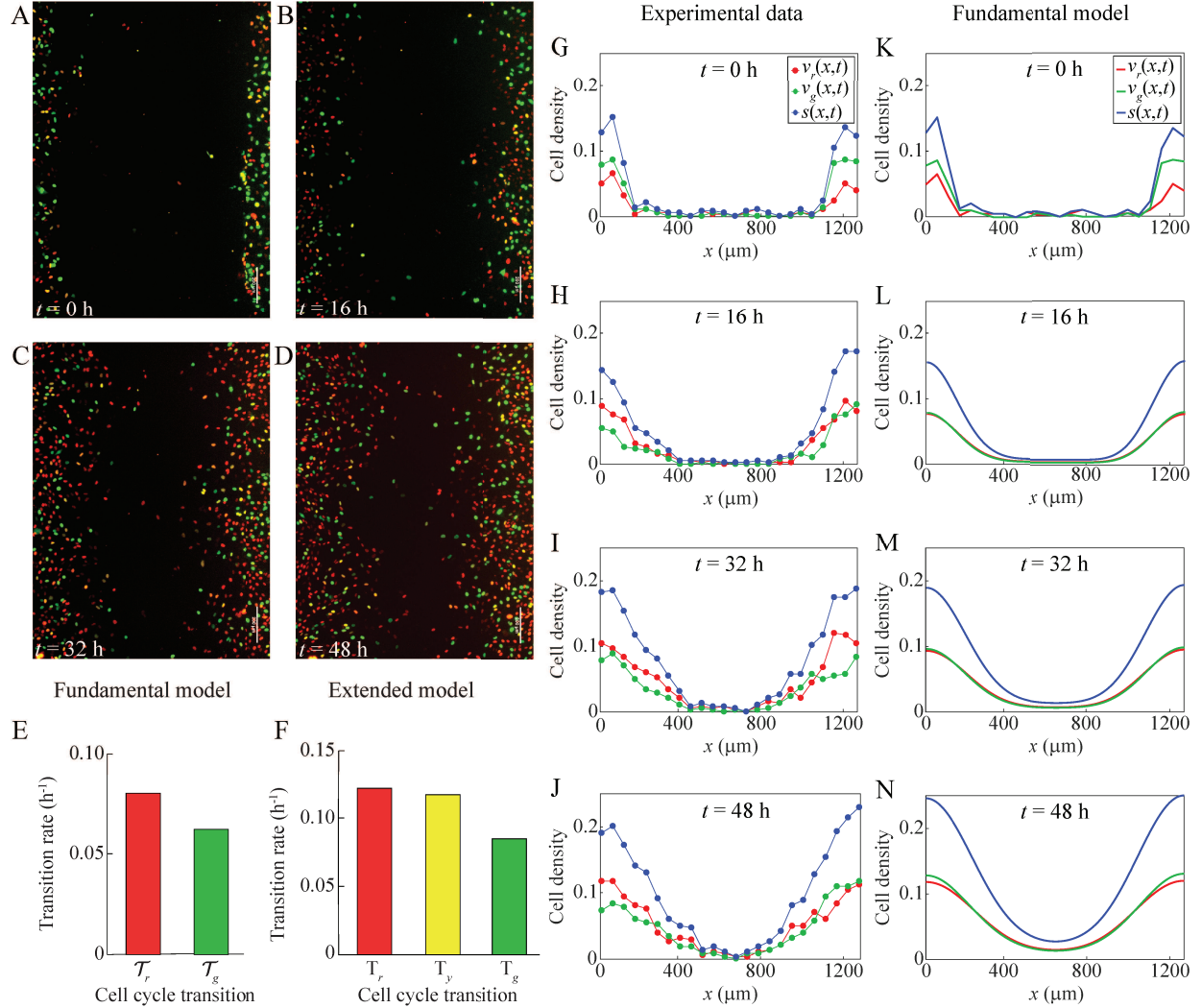


Figure S1: Comparison of experimental data and the fundamental model for a scratch assay of FUCCI-transduced WM983C melanoma cells. (A)–(D) Still images of a scratch assay with FUCCI-transduced WM983C melanoma cells at time 0 h, 16 h, 32 h and 48 h, respectively. Scale bar is $200 \mu\text{m}$. (E) Estimated transition rates from one cell cycle phase to the next for the fundamental model with two subpopulations, based on data from the WM983C cell line from Fig 1C in [2]. (F) Estimated transition rates from one cell cycle phase to the next for the extended model with three subpopulations, based on data from the WM983C cell line from Fig 1C in [2]. (G)–(J) Experimental non-dimensional cell density data at 0 h, 16 h, 32 h and 48 h, respectively (based on images (A)–(D)). The cell density is treated as a function of x and t only, owing to the fact that the initial density does not depend on the vertical coordinate, y . (K)–(N) Numerical solutions of the fundamental model, Eqs (2)–(3), at 0 h, 16 h, 32 h and 48 h. The numerical solutions are obtained with $\Delta x = 0.1 \mu\text{m}$, $\Delta t = 0.1 \text{ h}$, $L = 1254 \mu\text{m}$, diffusion coefficients $\mathcal{D}_r = \mathcal{D}_g = 400 \mu\text{m}^2 \text{ h}^{-1}$, transition rates $\kappa_r = 0.080 \text{ h}^{-1}$ and $\kappa_g = 0.062 \text{ h}^{-1}$, and initial conditions the same as for the experimental data.

3 Numerical solutions demonstrating travelling wave behaviour for the fundamental model when $\mathcal{D} \neq 1$.

In Fig S2 we present numerical solutions of the fundamental model, Eqs (2)–(3), with $\mathcal{D} \neq 1$. In Fig S2A, $\mathcal{D} = 0.5$, and in Fig S2B, $\mathcal{D} = 2$. These solutions are qualitatively the same as for $\mathcal{D} = 1$, see Fig 3, demonstrating that the existence of these travelling waves is robust, and does not depend on the value of $\mathcal{D}_g/\mathcal{D}_r$.

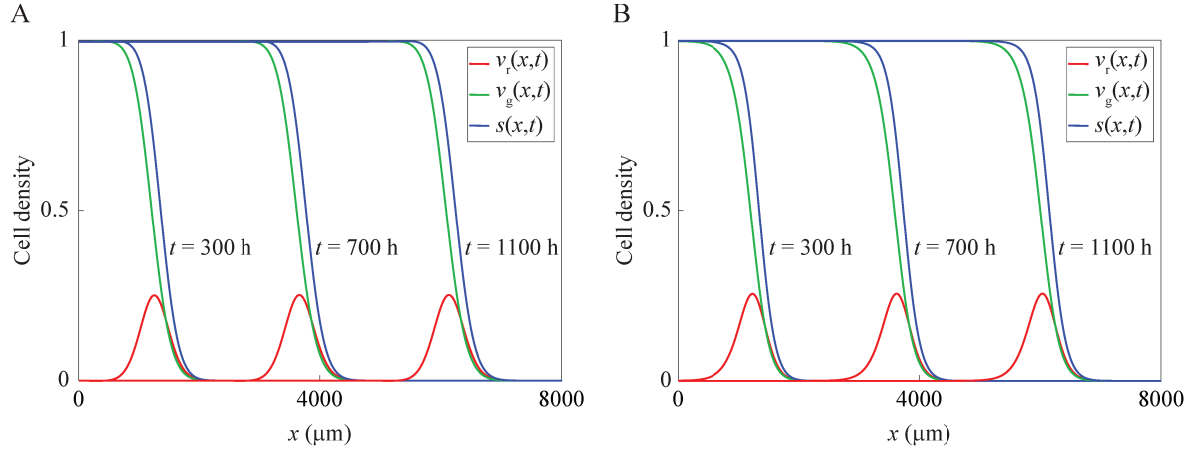


Figure S2: Numerical solutions of the fundamental model, Eqs (2)–(3), demonstrating travelling wave behaviour with $\mathcal{D} \neq 1$. (A) Solutions obtained with $\Delta x = 0.1 \mu\text{m}$, $\Delta t = 0.1 \text{ h}$, $L = 8000 \mu\text{m}$, $\mathcal{D}_r = 400 \mu\text{m}^2 \text{ h}^{-1}$, $\mathcal{D}_g = 200 \mu\text{m}^2 \text{ h}^{-1}$, $\kappa_r = \kappa_g = 0.08 \text{ h}^{-1}$, and the initial condition given by Eq (9) with $\xi = 10$. (B) Solutions obtained with $\Delta x = 0.1 \mu\text{m}$, $\Delta t = 0.1 \text{ h}$, $L = 8000 \mu\text{m}$, $\mathcal{D}_r = 200 \mu\text{m}^2 \text{ h}^{-1}$, $\mathcal{D}_g = 400 \mu\text{m}^2 \text{ h}^{-1}$, $\kappa_r = \kappa_g = 0.08 \text{ h}^{-1}$, and the initial condition given by Eq (9) with $\xi = 10$.

References

- [1] Morton, K. W. and D. F. Mayers, 2005. Numerical Solution of Partial Differential Equations. 2nd ed. Cambridge: Cambridge University Press.
- [2] Haass, N. K., K. A. Beaumont, D. S. Hill, A. Anfosso, P. Mrass, M. A. Munoz, I. Kinjyo, and W. Weninger, 2014. Real-time cell cycle imaging during melanoma growth, invasion, and drug response. *Pigment Cell Melanoma Res.* 27:764–776.